# MSFEM for the Eddy Current Problem in a Laminated Core Including Hysteresis

Markus Schöbinger[1], Simon Steentjes[2], Joachim Schöberl[1], Kay Hameyer[3], and Karl Hollaus[1]

[1]Institute for Analysis and Scientific Computing, Technische Universität Wien, 1040 Vienna, Austria
[2]AUDI AG, D-85045 Ingolstadt, Germany
[3]Institute of Electrical Machines (IEM), RWTH Aachen University, 52062 Aachen, Germany

**A multiscale finite-element method is extended to allow for materials with hysteresis. The method is developed for an eddy current problem, coupled with a network. As an example, a laminated toroidal transformer core is considered. Utilizing the symmetry of the domain, the problem can be rewritten as a 2-D one. The multiscale method shows good results compared to the reference solutions for both the nonlinear problem with magnetization curve and with the inclusion of hysteresis by the Preisach model while preserving its main advantages of drastically reducing the number of degrees of freedom by utilizing a coarse mesh that does not resolve each single iron sheet. Both the multiscale solution and the reference solution are compared to measurement data. It is demonstrated that the inclusion of hysteresis is necessary in order to achieve a good approximation of the measurement data, which is used to identify both the magnetization curve and the parameters for the Preisach model.**

*Index Terms*— **Eddy currents, hysteresis, laminates, multiscale finite-element method (MSFEM), network coupling, Preisach model.**

## I. Introduction

THE multiscale finite-element method (MSFEM) described in [1] has already been applied successfully to the linear and nonlinear eddy current problems (see [2] and [3]). Its main advantage is to greatly reduce the number of degrees of freedom in the finite-element system by allowing the usage of a coarse mesh, which does not resolve each individual iron sheet in the simulated core. The aim of this paper is to study a possibility to include hysteresis by the Preisach model.

The method is developed in the setting of the eddy current problem including network coupling with a voltage-driven coil. Using the **A** formulation, this kind of coupling has been presented in [4]. A variant using the $\mathbf{T}-\Phi$ formulation has later been presented in [5]. A discussion of the different formulations and the treatment of coils can be found in [6]. In this paper, the **A** formulation is used.

The developed method is tested by a numerical example. A toroidal transformer is simulated for which measurement data are available. As a simplification, only the core itself is considered in the simulated domain because experience has shown that the surrounding air can be neglected for this problem. The windings are evenly distributed around the core and assumed to be radially aligned. In the model, they are considered by a surface current density. An external circuit with a voltage source is coupled via this surface current density with the field problem. The cross section of the core is rectangular. These simplifications make it possible to restrict the full problem to a 2-D one using cylindrical coordinates.

Manuscript received November 5, 2018; revised February 21, 2019; accepted March 23, 2019. Date of publication April 29, 2019; date of current version July 18, 2019. Corresponding author: M. Schöbinger (e-mail: markus.schoebinger@tuwien.ac.at).

Color versions of one or more of the figures in this letter are available online at http://ieeexplore.ieee.org.

Digital Object Identifier 10.1109/TMAG.2019.2907894

The simulation results demonstrate that the chosen simplifications do not introduce significant errors. The MSFEM solution shows only a very small error compared to the reference solution even in this highly nonlinear setting.

## II. Eddy Current Problem With Circuit Coupling

Consider an eddy current problem with circuit coupling for the **A** formulation, as developed in [4]. In the time domain, it is given as: for a given voltage $u(t)$, find the current $i(t)$ and the magnetic vector potential $\mathbf{A}(t) \in H(\mathrm{curl})$ for all times $t \in \mathbb{R}^+$, so that

$$\int_\Omega \mu^{-1}(\mathbf{A})\mathrm{curl}\mathbf{A}\,\mathrm{curl}\mathbf{v} + \frac{\partial}{\partial t}\sigma\mathbf{A}\mathbf{v}\int d\Omega = \int_\Gamma i\mathbf{v}\boldsymbol{\tau}_\mathrm{N}\int d\Gamma$$
$$iR + \int_\Gamma \frac{\partial}{\partial t}\mathbf{A}\boldsymbol{\tau}_\mathrm{N}\int d\Gamma = u \tag{1}$$

for all $\mathbf{v} \in H(\mathrm{curl})$ with $\boldsymbol{\tau}_\mathrm{N}$ being the winding density. The vector potential **A** is chosen to fulfill homogenous Neumann boundary conditions on $\partial\Omega$. The coefficients in (1) are the magnetic permeability $\mu$, the electric conductivity $\sigma$, and the electric resistance $R$ of the primary winding.

## III. Simplification of the Problem

In this paper, a toroidal transformer with a laminated core is considered. The isolating layers between the iron sheets are considered as air gaps. Using cylindrical coordinates, the domain can be written as $\Omega = [r_1, r_2] \times [0, 2\pi] \times [-(h/2), (h/2)]$, with $r_1, r_2$, and $h$ denoting the inner radius, the outer radius, and the total height of the core, respectively.

In this setting, the winding density is given as

$$\boldsymbol{\tau}_\mathrm{N} := \frac{N}{2\pi r}\boldsymbol{\tau} \tag{2}$$

where $\boldsymbol{\tau}$ is the unit tangential vector on the boundary of a cross section of the core (see Fig. 1), $r$ is the radial coordinate, and $N$ is the number of the primary windings.

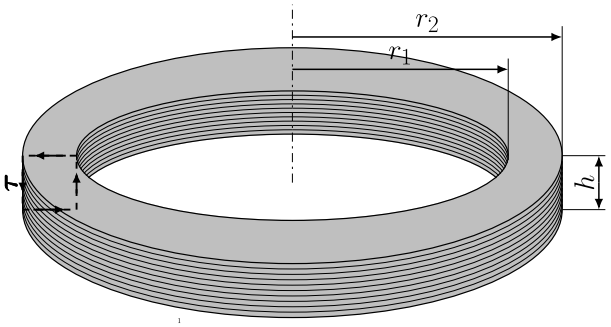


Fig. 1. Laminated toroidal core and the unit tangential vector $\vec{\tau}$ of the cross section of the core (dashed line).

To reduce the computational effort needed to solve (1) on the 3-D domain $\Omega$, the system is rewritten to a simpler problem.

It is reasonable to assume that the solution does not depend on the angle $\varphi$. Because the windings are assumed to be aligned with the radius, $\mathbf{A}$ does not have a component in the azimuthal direction. This allows for the simplification

$$\mathbf{A} = \begin{pmatrix} A_\mathrm{r}(r,\varphi,z) \\ A_\varphi(r,\varphi,z) \\ A_\mathrm{z}(r,\varphi,z) \end{pmatrix} = \begin{pmatrix} A_\mathrm{r}(r,z) \\ 0 \\ A_\mathrm{z}(r,z) \end{pmatrix}. \tag{3}$$

As a result, the curl in cylindrical coordinates becomes

$$\mathrm{curl}\mathbf{A} = \begin{pmatrix} \frac{1}{r}\frac{\partial A_\mathrm{z}}{\partial \varphi} - \frac{\partial A_\varphi}{\partial z} \\ \frac{\partial A_\mathrm{r}}{\partial z} - \frac{\partial A_\mathrm{z}}{\partial r} \\ \frac{1}{r}\left(\frac{\partial (rA_\varphi)}{\partial r} - \frac{\partial A_\mathrm{r}}{\partial \varphi}\right) \end{pmatrix} = \begin{pmatrix} 0 \\ \frac{\partial A_\mathrm{r}}{\partial z} - \frac{\partial A_\mathrm{z}}{\partial r} \\ 0 \end{pmatrix}. \tag{4}$$

By defining the curl operator in two dimensions as the scalar function

$$\mathrm{curl}\begin{pmatrix} u_\mathrm{r}(r,z) \\ u_\mathrm{z}(r,z) \end{pmatrix} := \frac{\partial u_\mathrm{z}}{\partial r} - \frac{\partial u_\mathrm{r}}{\partial z} \tag{5}$$

the problem can be reformulated on the 2-D domain $\Omega_{2\text{-D}} = [r_1, r_2] \times [-(h/2), (h/2)]$, corresponding to a cross section of the core at an arbitrary angle $\varphi$. Details about the implementation of this 2-D $H(\mathrm{curl})$ space can be found in [7].

To obtain a unified equation system for both unknowns $(\mathbf{A}, i)$, the second equation in (1) is also treated in the weak sense by multiplying it with a constant test function $j$. Furthermore, the time dependence is solved by a time-stepping method using the implicit Euler method, i.e., for a time step $\Delta t$ approximating

$$\frac{\partial}{\partial t}\mathbf{A} \approx \frac{\mathbf{A}^{k+1} - \mathbf{A}^k}{\Delta t} \tag{6}$$

with the superscripts denoting the current time instant and solving for $\mathbf{A}^{k+1}$ in each time instant.

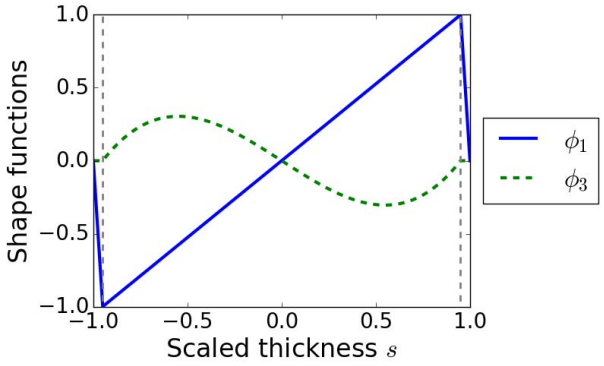


Fig. 2. Polynomial shape functions over the thickness of one iron sheet with an air gap, scaled to the interval $[-1, 1]$. The gray dashed lines mark the boundaries of the iron sheet.

The final problem is given as: given $u^{k+1}$, find $i^{k+1} \in \mathbb{R}$ and $\mathbf{A}^{k+1}(t) \in H(\mathrm{curl})$, so that

$$\begin{aligned} &\int_{\Omega_{2\text{-D}}} \mu^{-1}(\mathbf{A}^{k+1})\mathrm{curl}\mathbf{A}^{k+1}\,\mathrm{curl}\mathbf{v} \\ &\quad + \frac{1}{\Delta t}\sigma \mathbf{A}^{k+1}\mathbf{v}\,\mathrm{d}\Omega_{2\text{-D}} - \int_{\Gamma_{2\text{-D}}} i^{k+1}\mathbf{v}\boldsymbol{\tau}_N\,\mathrm{d}\Gamma_{2\text{-D}} \\ &\quad = \int_{\Omega_{2\text{-D}}} \frac{1}{\Delta t}\sigma \mathbf{A}^k\mathbf{v}\,\mathrm{d}\Omega_{2\text{-D}} \\ &\qquad \int_{\Gamma_{2\text{-D}}} \mathbf{A}^{k+1}\boldsymbol{\tau}_N j\,\mathrm{d}\Gamma_{2\text{-D}} + \Delta t i^{k+1} R j \\ &\quad = \int_{\Gamma_{2\text{-D}}} \mathbf{A}^k\boldsymbol{\tau}_N j\,\mathrm{d}\Gamma_{2\text{-D}} + \Delta t u^{k+1} j \end{aligned} \tag{7}$$

for all $\mathbf{v} \in H(\mathrm{curl})$ and all $j \in \mathbb{R}$. Note that the curl operator in (7) refers to the 2-D curl given in (5).

Under the chosen assumptions on the geometry, (7) is equivalent to the original problem (1). The fixed point iteration method described in [8] is used to solve the nonlinear problem (7).

## IV. Multiscale Method

In order to reduce the number of unknowns in the resulting finite-element equation system, the multiscale method described in [1] is used. The idea is to approximate the solution by the multiscale approach

$$\mathbf{A} \approx \mathbf{A}_0 + \phi_1(z)\begin{pmatrix} A_1 \\ 0 \end{pmatrix} + \nabla(\phi_1(z)w_1) \tag{8}$$

with the three auxiliary functions $\mathbf{A}_0 \in H(\mathrm{curl})$, $A_1 \in L_2$, and $w \in H^1$ becoming the new unknowns.

The local behavior is recovered by the micro-shape function $\phi_1$, which is a continuous piecewise linear function that increases from $-1$ to 1 over the thickness of one iron sheet and decreases back to $-1$ in each air gap (see Fig. 2).

The MSFEM equation system is obtained by using the ansatz (8) in (7) together with the similar expansion

$$\mathbf{v} \approx \mathbf{v}_0 + \phi_1(z)\begin{pmatrix} v_1 \\ 0 \end{pmatrix} + \nabla(\phi_1(z)q_1) \tag{9}$$

for the test function. Straightforward calculations yield, in each time step, the multiscale problem: given the same parameters

as in (1) and the solution of the previous time step, find $\mathbf{A}_0^{k+1} \in H(\mathrm{curl})$, $A_1^{k+1} \in L_2$, $w^{k+1} \in H^1$, and $i^{k+1} \in \mathbb{R}$ so that

$$\begin{aligned}
&\int_{\Omega_{2\text{-D}}} \overline{\mu^{-1}(\mathbf{A}^{k+1})}\mathrm{curl}\mathbf{A}_0^{k+1}\,\mathrm{curl}\mathbf{v}_0 \\
&\quad -\overline{\mu^{-1}(\mathbf{A}^{k+1})\phi_{1,z}}\left(\mathrm{curl}\mathbf{A}_0^{k+1}v_1 + A_1^{k+1}\mathrm{curl}\mathbf{v}_0\right) \\
&\quad +\overline{\mu^{-1}(\mathbf{A}^{k+1})\phi_{1,z}^2}A_1^{k+1}v_1 \\
&\quad +\frac{1}{\Delta t}\left(\overline{\sigma}\mathbf{A}_0^{k+1}\mathbf{v}_0 + \overline{\sigma\phi_{1,z}^2}w^{k+1}q\right. \\
&\quad +\overline{\sigma\phi_{1,z}}\left(\mathbf{A}^{k+1}q + w^{k+1}\mathbf{v}_0\right) \\
&\quad +\overline{\sigma\phi^2}(\nabla w^{k+1}\nabla q + A_1^{k+1}v_1) \\
&\quad \left.+\overline{\sigma\phi^2}(A_1^{k+1}\frac{\partial}{\partial r}q + \frac{\partial}{\partial r}w^{k+1}v_1)\right)\mathrm{d}\Omega_{2\text{-D}} \\
&-\int_{\Gamma_{2\text{-D}}} i^{k+1}\mathbf{v}_0\boldsymbol{\tau}_N \int d\Gamma_{2\text{-D}} = \int_{\Omega_{2\text{-D}}} \frac{1}{\Delta t}\sigma\mathbf{A}_0^k\mathbf{v}_0\,\mathrm{d}\Omega_{2\text{-D}} \\
&\int_{\Gamma_{2\text{-D}}} \mathbf{A}_0^{k+1}\boldsymbol{\tau}_N j\,\mathrm{d}\Gamma_{2\text{-D}} + \Delta t i^{k+1}Rj \\
&= \int_{\Gamma_{2\text{-D}}} \mathbf{A}_0^k\boldsymbol{\tau}_N j\,\mathrm{d}\Gamma_{2\text{-D}} + \Delta t u^{k+1}j \qquad (10)
\end{aligned}$$

for all $\mathbf{v}_0 \in H(\mathrm{curl})$, $v_1 \in L_2$, $q \in H^1$, and $j \in \mathbb{R}$ and with $\phi_{1,z}$ denoting the derivative of $\phi_1$ with respect to $z$.

For linear expressions (i.e., those containing $\sigma$ and, in the case of a linear material model, also $\mu$), a bar indicates that the respective coefficient is averaged over the thickness of one iron sheet plus one air gap, as described in [1]. The advantage of these new functions is that they represent coefficients that vary only on a large scale, i.e., they show little variation on the scale of the sheet thickness. Therefore, the mesh on which they are solved for does not need to resolve each individual iron sheet, allowing for a significant reduction in finite elements. The treatment of nonlinear expressions, which cannot be globally precomputed, is described in Section V.

The lowest order approach (8) can be expanded to increase the quality of the approximation. In this paper, the third-order expansion

$$\mathbf{A} \approx \mathbf{A}_0 + \phi_1\begin{pmatrix}A_1\\0\end{pmatrix} + \nabla(\phi_1 w_1) + \phi_3\begin{pmatrix}A_3\\0\end{pmatrix} + \nabla(\phi_3 w_3) \qquad (11)$$

is also used and compared to the lowest order method. The derivation of the corresponding weak problem is analogous to that for (10) and is not presented for reasons of brevity.

## V. Implementation of Material Models

In this paper, the performance of the MSFEM compared to the standard FEM is investigated for two different material models: a nonlinear magnetic reluctivity and a hysteretic relation between $\mathbf{H}$ and $\mathbf{B}$. The case of a linear relation $\mathbf{B} = \mu_{\mathrm{FE}}\mathbf{H}$ in iron with some constant value $\mu_{\mathrm{FE}}$ has already been tested extensively (see [1]–[3]). Therefore, it is not discussed in this paper.

Note that the models presented in this sections are scalar, i.e., $\mathbf{B}$ and $\mathbf{H}$ are assumed to have only an azimuthal component perpendicular to the cross section of the core. In the following, we will use the scalar properties $H := \mathbf{H}\cdot\mathbf{e}_\varphi$ and $B := \mathbf{B}\cdot\mathbf{e}_\varphi$.

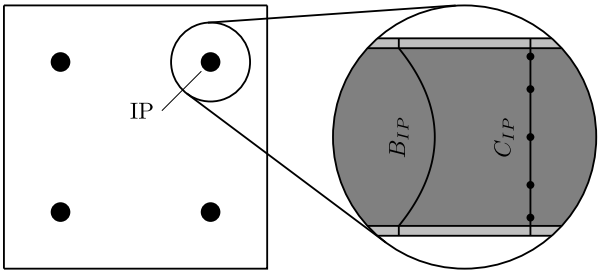


Fig. 3. Each IP in each finite element is assigned a 1-D reference cell $C_{\mathrm{IP}}$ consisting of the iron sheet (dark gray) and the air gap (light gray). The field $B_{\mathrm{IP}}$ and the coefficients derived from it are averaged using numeric integration.

As the first step, a nonlinear relationship between $B$ and $H$ is considered. In the presented examples, the used $B$–$H$ curve is obtained by a linear interpolation of the measurement data. For the standard FEM, this leads to a nonlinear system of equations in each time instant.

In the lowest order MSFEM setting (8), the obtained $B$ field has the form

$$B = \mathrm{curl}\mathbf{A} = \mathrm{curl}\mathbf{A}_0 - \phi_{1,z}A_1. \qquad (12)$$

The nonlinear coefficients in (10) are treated by a variant of the method described in [3]. Each integration point (IP) used in the assembling of the FEM matrix is assigned a 1-D reference cell $C_{\mathrm{IP}}$ consisting of one iron sheet and one-half of an air gap to both sides (see Fig. 3). The $B$ field on that cell is approximated by a field $B_{\mathrm{IP}}$ that is calculated by (12) with $\mathbf{A}_0$ and $A_1$ being replaced by their evaluated values at IP. Because $\phi_{1,z}$ is a piecewise constant function, $B_{\mathrm{IP}}$ and, by extension, $\mu = \mu(B_{\mathrm{IP}})$ are also piecewise constant on $C_{\mathrm{IP}}$. In this case, the averages in (10) can be calculated with the formulas used in the linear setting, applied to each IP individually, which implies no additional overhead compared to the standard FEM.

In the case of the third-order MSFEM (11), the $B$ field is given as

$$B = \mathrm{curl}\mathbf{A} = \mathrm{curl}\mathbf{A}_0 - \phi_{1,z}A_1 - \phi_{3,z}A_3 \qquad (13)$$

with the term $\phi_{3,z}$ being a quadratic polynomial in $z$, i.e., the $B_{\mathrm{IP}}$ field is not constant in the iron sheet anymore. Here, the averages are calculated using numerical integration on the iron sheet of each reference cell $C_{\mathrm{IP}}$ by a suitable number of Gaussian points. This results in additional work in the assembling of the FEM matrix but preserves the main advantage of MSFEM, namely, the low number of equations in the final system. Note that $\mu$ and $B_{\mathrm{IP}}$ are constant in the air gap. Consequently, no numerical integration is needed there.

The last step is the implementation of a hysteresis model. There exists a wide variety of models and the applicability of several different ones is studied in [9]. In this paper, the Preisach model was chosen.

As described, for example, in [10], the Preisach model gives a relationship between $H$ and $B$, which depends on past states of the system. The basic principle is that the past extrema of

the input $H$ define a staircase line in the triangular Preisach plane or Preisach triangle. The output $B$ is given by the integral of a given distribution function over the Preisach triangle with the sign of the distribution function $P$ being determined by the staircase line.

For the implementation, it is much more practical to work with the Everett function, which gives the integral of the distribution function over a subtriangle of the entire domain (see [11]).

Because an implementation of the complete Preisach model would require measurement data for a high number of first-order reversal curves, which were not available, a variant was chosen, which gives an approximation of the model based on the major hysteresis loop. This will, of course, affect the precision of the simulations compared to measurement data. However, as demonstrated in Section VI, the hysteretic behavior is still captured with reasonable accuracy. The focus of this paper is to show the compatibility of the proposed MSFEM with the Preisach model, which is independent of the specific choice for the Preisach distribution function.

A Lorentzian Preisach distribution function as described in [12] was used. It has the form

$$P(\alpha,\beta) = \frac{K_1}{\left(1+\left(\frac{\alpha-a}{b}\right)^2\right)\left(1+\left(\frac{\beta+a}{b}\right)^2\right)} + \delta(\alpha-\beta)\left(\frac{K_2}{\left(1+\left(\frac{\alpha}{e}\right)^2\right)}+f\right) \tag{14}$$

where $a, b, K_1, K_2, e$, and $f$ are the generic constants, which are determined by a least square fitting method and $\delta$ denotes the Dirac delta function. A sufficient condition to ensure $P(\alpha,\beta) \geq 0$ for all $\alpha$ and $\beta$ is $K_1, K_2, f \geq 0$.

The Everett function resulting from (14) is given as

$$E(\alpha,\beta) = K_1 b^2 \mathrm{at}\left(\frac{\beta+a}{b}\right)\left(\mathrm{at}\left(\frac{\beta-a}{b}\right)-\mathrm{at}\left(\frac{\alpha-a}{b}\right)\right) + K_2 e\left(\mathrm{at}\left(\frac{\beta}{e}\right)-\mathrm{at}\left(\frac{\alpha}{e}\right)\right)+f(\beta-\alpha) - \int_\alpha^\beta \frac{K_1 b^3 \mathrm{at}\left(\frac{\xi+a}{b}\right)}{\xi^2-2a\xi+a^2+b^2}\,d\xi \tag{15}$$

where at was written instead of arctan to preserve space. The remaining integral in (15) does not have an analytic representation and has to be calculated numerically. To increase the computational efficiency, the Everett function is computed on a high number of grid points in the Preisach triangle beforehand. Later evaluations are calculated from quadratic interpolation of these precomputed data.

Also, note that common hysteresis models, including the presented one, give the relationship between the fields in the form $B = B(H)$, i.e., $H$ is the input used to calculate $B$. This is in contrast to the problem at hand where $B = \mathrm{curl}\mathbf{A}$ is given and $H$ has to be calculated. To account for this, the model has to be inverted. More precisely, one has to solve the problem: given the pair of old fields $H_0$ and $B_0$ and the new target value $\hat{B}$, find the corresponding input value $\hat{H}$ for which the hysteresis model reproduces the output $\hat{B}$. An overview of algorithms for this problem can be found, for example, in [13].

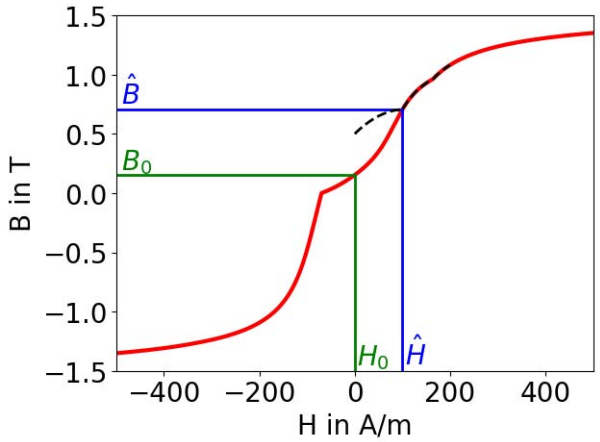


Fig. 4. $B$–$H$ curve obtained by the initial point $(H_0, B_0)$ and a certain history, varying the input $H$. The history was artificially chosen to accentuate the discontinuities in the first derivative. After the update to the new state $(H_1, B_1)$, a new $B$–$H$ curve is obtained, indicated by the black dashed line.

In the implementation used in this paper, the inversion was realized by utilizing that for a smooth Preisach distribution function $P$, the current input–output pair $(H_0, B_0)$ at a fixed time together with the stored history of past extrema of $H$ generates a continuous, monotone, piecewise smooth $B$–$H$ curve when considering all possible new input values $H$ (see Fig. 4). This curve is used in the nonlinear solver until a new pair $(H_1, B_1)$ with $|B_1 - \hat{B}| < \varepsilon$ is found for a given tolerance $\varepsilon$. This new input is then used to obtain the curve for the next time step, see the dashed line in Fig. 4.

The discontinuities in the first derivative of these curves coincide with the stored past extrema of $H$. These, in turn, coincide with the steps of the staircase line in the Preisach plane (see Fig. 5). Because of these discontinuities, Newton's method cannot be used directly to solve for $\hat{H}$. As a first step, the past extrema that give the best upper and lower bounds for $\hat{H}$ need to found. This limits the search to an interval where the curve is smooth and Newton's method can be used.

Another problem when dealing with hysteresis is that while the fields $H$ and $B$ are connected in a continuous way, the derived property needed in the FEM system, i.e., $\nu = \mu^{-1} = (H/B)$ has a singularity whenever $B$ changes its sign, resulting in numerical instabilities. One way to deal with this problem is to take the derivative with respect to time in the original equations (1). This leads to a structurally identical problem, except the right-hand side is now given by the time variation of the voltage instead of the voltage itself, instead of $i$ and $\mathbf{A}$, one solves for the time derivatives of these properties and the reluctivity is replaced by the differential reluctivity $\nu_d = (\partial H)/(\partial B)$. The original properties may easily be recovered by discretely integrating their calculated time derivatives with respect to time, and the new system has the benefit that the differential reluctivity behaves as a bounded, positive function everywhere. This has already been made use of, for example, in [14].

The application of the hysteresis model to the MSFEM is essentially identical to the nonlinear case. For the lowest order

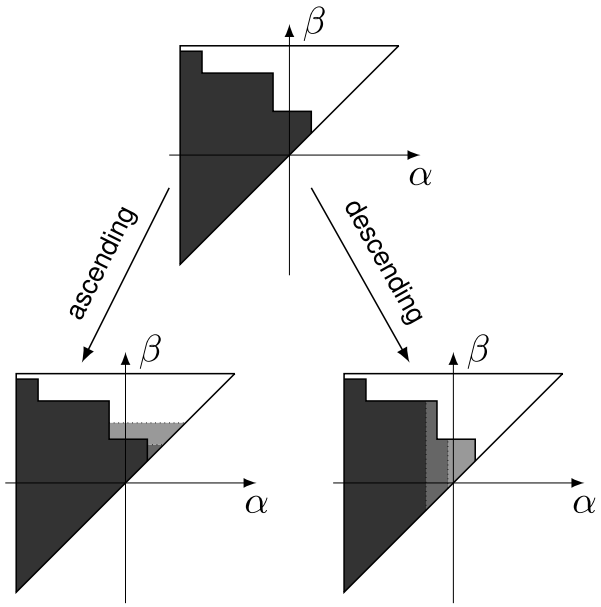


Fig. 5. State of the Preisach model at $(H_0, B_0)$ and its change with ascending and descending input $H$. Because $B$ is given by the integral of the distribution function underneath the staircase line, the derivative of $B$ becomes discontinuous every time the change in the area passes one of the original steps.

MSFEM, only a single Preisach model has to be implemented for each IP because $B$ is constant in iron on each reference cell. For the higher order MSFEM, each point in the reference cell $C_{\mathrm{IP}}$ of each IP, where the field $B_{\mathrm{IP}}$ is evaluated, is equipped with a separate Preisach model and the averaged properties are again approximated using numerical integration.

## VI. Numerical Results

A real transformer with available measurement data is used as a numerical example. Its outer radius is given as $r_2 = 30$ mm, its inner radius as $r_1 = 24$ mm, and the total height is $h = 5$ mm (see Fig. 1. It consists of ten iron sheets, each 0.5 mm thick. In the available measurement data, the thickness of the air gap is not specified. For the simulations, an artificial thickness of 1% of one iron sheet is chosen. The setup consists of 75 primary windings and 81 secondary windings.

The experimental results were carried out on a ring core, which was incorporated within a computer-aided setup in accordance with the international standard IEC 60404-6. The ring core was characterized by using sinusoidal magnetic flux density with a form-factor error of less than 1%.

The electric conductivity is given as $\sigma = 2.06 \cdot 10^6$ S/m in iron. To obtain a numerically stable problem, an artificial conductivity of $\sigma = 1$ S/m is chosen in air. The electric resistance is $R = 86$ mΩ. The magnetic permeability is $\mu = \mu_0$ in air and chosen according to the respective model in iron. The prescribed voltage is $u(t) = U_{\max} \cos(2\pi f t)$ with the peak voltage $U_{\max}$. Most of the presented results were calculated for the frequency $f = 50$ Hz, with some comparisons to the case $f = 10$ Hz being given.

Note that the problem was defined on the 2-D domain $\Omega_{2\text{-D}}$. The meshes used for the standard FEM reference solution and the MSFEM solution are shown in Fig. 6. First-order finite elements were used in the calculations for the MSFEM and third-order finite elements for the reference solution. A total number of degrees of freedom for the MSFEM are 126 for the lowest order approach (8) and 189 with the inclusion of the third-order term (11). In comparison, the reference solution requires 29 653 degrees of freedom.

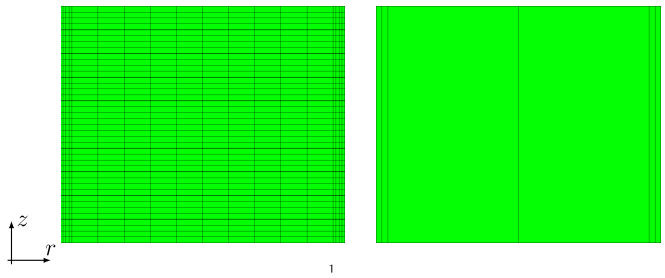


Fig. 6. Mesh for the reference solution (918 elements) and the MS (6 elements).

TABLE I
Preisach Parameters

| | 10 Hz | 50 Hz |
|---|---|---|
| $a$ | -5.65895187e+01 | -8.18773707e+01 |
| $b$ | 3.52032590e+01 | 4.13538892e+01 |
| $K_1$ | 1.72599749e-02 | 2.00442033e-02 |
| $K_2$ | 2.07211005e-01 | 2.49345353e-01 |
| $e$ | 1.32612003e+02 | 1.33306276e+02 |
| $f$ | 3.48025117e-03 | 5.57513398e-03 |

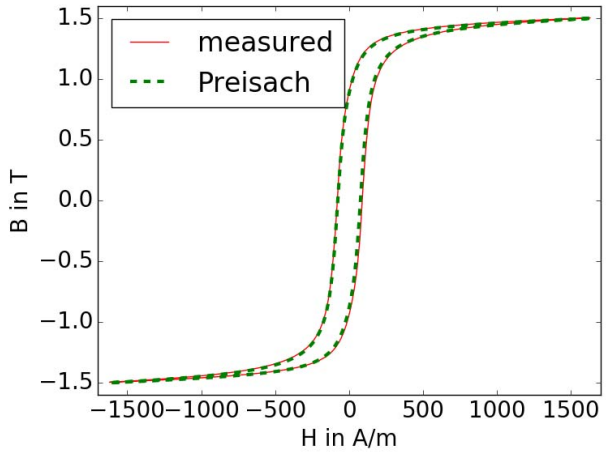


Fig. 7. Comparison of the measured major hysteresis loop and the approximation at 50 Hz.

The identified parameters for the Preisach distribution function (14), obtained by fitting the major hysteresis loop in the least square sense, are listed in Table I. Note that the chosen Preisach model is rate independent, but for each frequency, a different set of parameters was fit to take account of the rate-dependent effects somehow.

In Fig. 7, the measured major hysteresis loop at 50 Hz is compared to the one reconstructed by the Preisach model. It can be seen that the chosen distribution (14) gives a

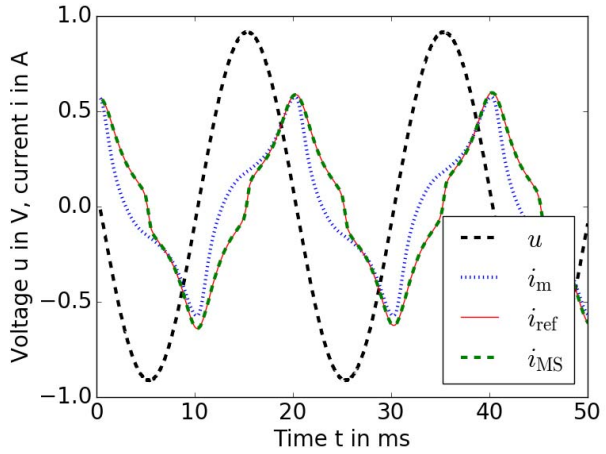


Fig. 8. Comparison of the current $I$ at a given voltage $U$ for the measurement data (m), the FEM reference solution (ref), and the MS for an average flux density of 1.2 T, using the nonlinear $B$–$H$ curve at 50 Hz.

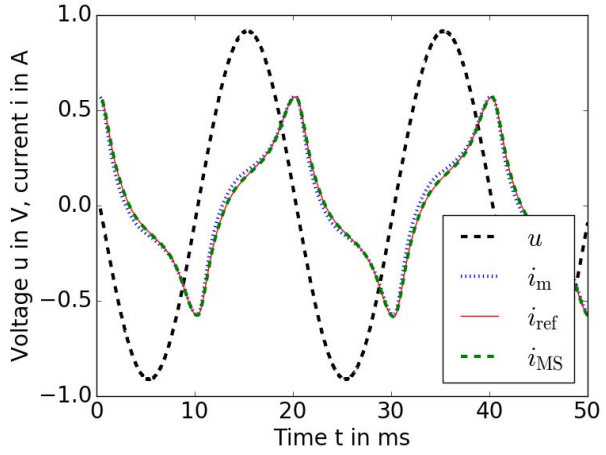


Fig. 9. Comparison of the current $I$ at a given voltage $U$ for the measurement data (m), the FEM reference solution (ref), and the MS for an average flux density of 1.2 T, using the Preisach model at 50 Hz.

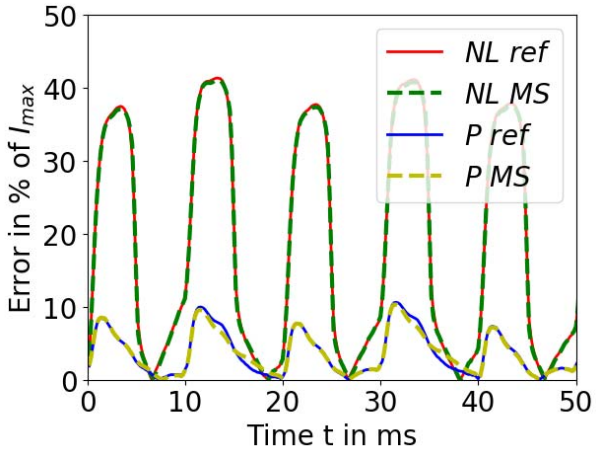


Fig. 10. Error in the calculated currents relative to the attained maximum current, comparing the nonlinear model (NL) and the Preisach model (P) for both the reference solution (ref) and the MS for an average flux density of 1.2 T and a frequency of 50 Hz.

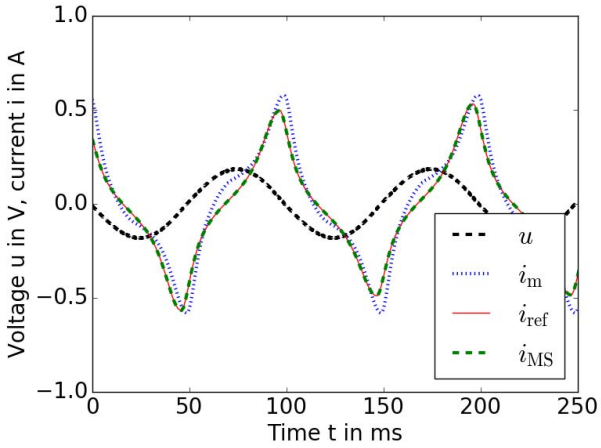


Fig. 11. Comparison of the current $I$ at a given voltage $U$ for the measurement data (m), the FEM reference solution (ref), and the MS for an average flux density of 1.2 T, using the Preisach model at 10 Hz.

good approximation of the measured major loop. For 10 Hz, the results are very similar.

The performance of the used methods is shown in Figs. 8 and 9, where an excitation frequency of 50 Hz is chosen and an average flux density of 1.2 T is obtained. The measurement data for the current are compared to the results of the simulations, using the nonlinear $B$–$H$ curve and the identified Preisach model, respectively. It can be seen easily that a hysteresis model is required to obtain a good approximation (see Fig. 10). The simple nonlinear method is only able to give a very rough approximation of the real current. The ability of the MSFEM method to approximate the reference solution, on the other hand, does not seem to be influenced by the model used for the nonlinearity. In Figs. 8–10, the calculated currents are virtually identical.

This also holds true for an excitation frequency of 10 Hz, as shown in Fig. 11. Here, the differences to the measurement data are more significant, but there is still a good agreement between the simulated current and the measured one.

In the following, the difference between the reference solution and the MSFEM solution is analyzed in more detail.

Three metrics are used to measure this difference: the error in the calculated current and the errors in the **B** and **J** fields. The latter are measured in the $L_2$-norm evaluated on the reference mesh. This is a much stricter, local measure of the error than the current, which is a global property. To ensure comparability of these properties and to prevent singularities when the reference solution switches signs, all errors are given as a percentage of the highest respective value of the reference solution, e.g., for the **J** field, we calculate in each time instant $t$

$$\mathrm{err}_{\mathbf{J}}(t) = \frac{\sqrt{\int_\Omega (\mathbf{J}_{MS}(t) - \mathbf{J}_{\mathrm{ref}}(t))^2 \, d\Omega}}{\max\limits_{s\in[0,T_{end}]} \sqrt{\int_\Omega \mathbf{J}_{\mathrm{ref}}(s)^2 \, d\Omega}} \cdot 100\%. \tag{16}$$

The results are shown in Figs. 12 and 13.

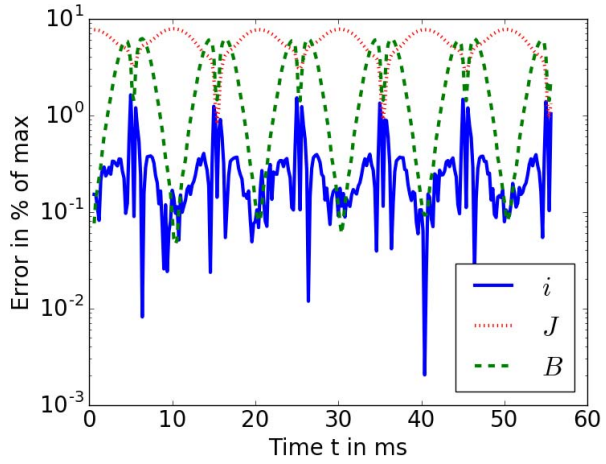


Fig. 12. Errors of the first-order MSFEM solution to the reference solution at an average flux density of 1.2 T, using the nonlinear $B$–$H$ curve at 50 Hz.

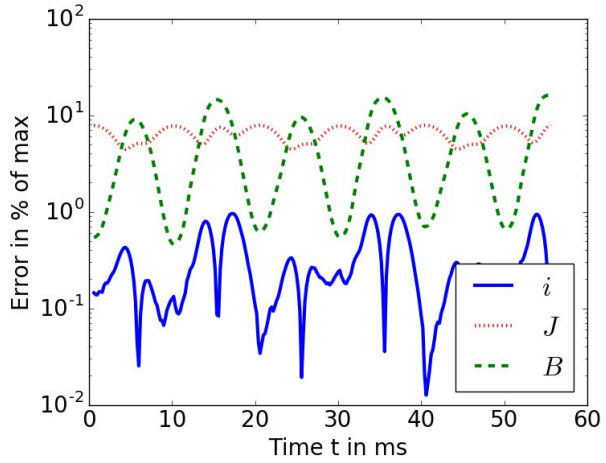


Fig. 13. Errors of the first-order MSFEM solution to the reference solution at an average flux density of 1.2 T, using the Preisach model at 50 Hz.

It is clearly visible that the total current is approximated better than the fields, with the error always staying below 1% using the Preisach model and admitting some peaks of about 2% in the nonlinear case. **J** shows a similar error pattern for both the nonlinear formulation and the formulation including hysteresis and the **B** field is resolved a bit better if there is no hysteresis. In both cases, the error in the **B** field varies strongly over each time period.

Note that (16) does not include the actual measurement data. The plots in Figs. 12 and 13 demonstrate that the material model does not significantly influence the ability of the multiscale solution (MS) to approximate the reference solution. Fig. 8 shows that the error with respect to the measurement data is strongly dependent on the chosen material model and affects both the reference solution and the MS equally.

Another way to measure the approximation quality is to compare the calculated losses. Three different kinds of losses are considered: the losses due to $R$

$$P_R = \frac{1}{T}\int_0^T \int_\Omega I(t)^2 R \, d\Omega \, dt \tag{17}$$

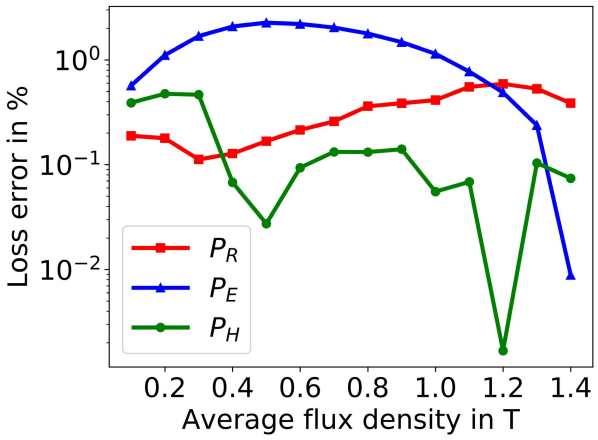


Fig. 14. Errors of the total losses computed by the complex simulation and the Preisach model compared to the reference solution over a range of average flux densities at 50 Hz.

the eddy current losses

$$P_E = \frac{1}{T}\int_0^T \int_\Omega \sigma \frac{\partial}{\partial t}\mathbf{A} \cdot \frac{\partial}{\partial t}\mathbf{A} \, d\Omega \, dt \tag{18}$$

and the hysteresis losses $P_H$, which, in general, are defined as the area inside the traversed hysteresis loop. For the Preisach model, there exists a generalization that allows for the calculation of losses even for not perfectly closed paths (see [15]).

In Fig. 14, the errors in the calculated losses are visualized. It can be seen that the MSFEM is able to correctly reproduce each component of the total losses with a maximum error lower than 3%.

If only the total losses over one time period are of interest, it is possible to run a simulation with a fictitious material (as described, for example, in [16]) and calculate the losses in a post-processing step via the formula

$$P = k_1 f B_{\max}^2 + k_2 f^2 B_{\max}^2 \tag{19}$$

with the parameters $k_1$ and $k_2$ being obtained by fitting to measurement data. This approach is compared to the total losses obtained by the Preisach model, as shown in Fig. 15. It can be seen that the accuracy of these two models is comparable, with the Preisach model giving significantly better results for lower flux densities. It should be noted that the simulation with the fictitious material, while being computationally cheaper, does not provide the development of the losses over time.

To increase the accuracy of the MS, one could use the third-order MSFEM (11) instead of the first-order method (8). In Fig. 16, a snapshot in time of the calculated **J** and **B** fields is shown for both the first- and third-order MSFEMs and the reference solution of the problem including the Preisach model. Note that all solutions are drawn on the reference mesh.

There is a clear increase in quality when including the third-order terms. In the **J** field, the boundary effects are much better resolved, and for the **B** field, the higher order terms are necessary to include the behavior of the solution inside an iron sheet instead of giving only an estimation of the mean

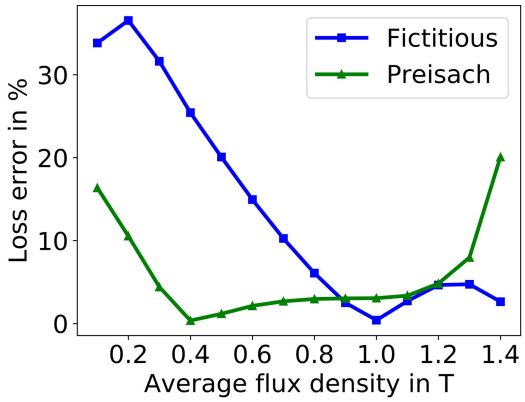


Fig. 15. Errors of the losses computed by the MSFEM solution compared to the measurement data over a range of average flux densities at 50 Hz.

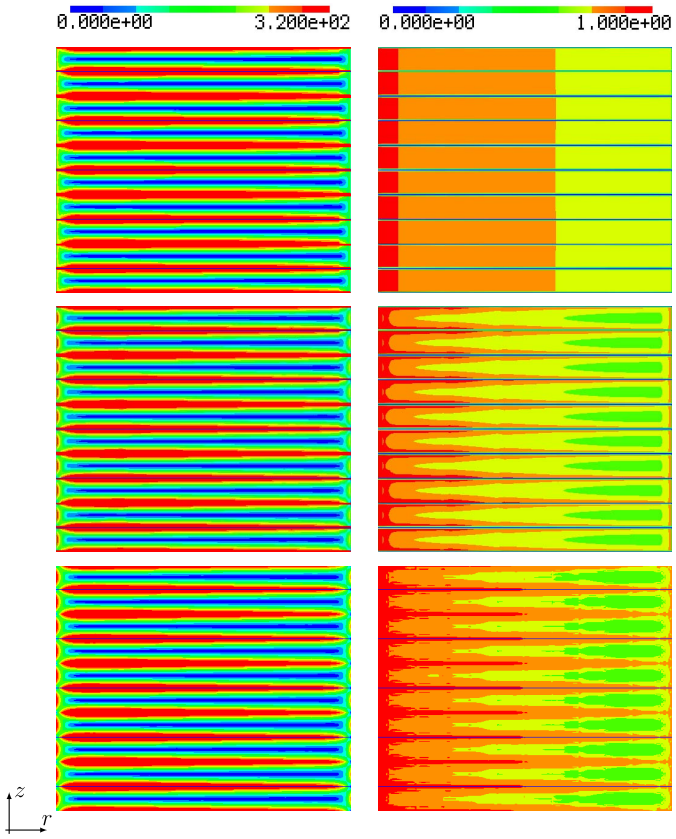


Fig. 16. Absolute value of the **J** (left) and **B** (right) fields at $t = 17.2$ ms for the first-order MSFEM, third-order MSFEM, and the reference solution (from top to bottom), using the Preisach model at 50 Hz and an average flux density of 1.2 T.

value. To quantify this improvement, a range of average flux densities is considered, and for each, the average errors over the entire time interval are calculated. The results can be seen in Figs. 17 and 18.

The inclusion of the third-order terms allows for a consistent reduction of the relative error for all measured quantities, which is greater in the case of a simple nonlinearity, but even using hysteresis, the errors are still decreased by a factor of 2. Figs. 17 and 18 also illustrate the error being smaller for low

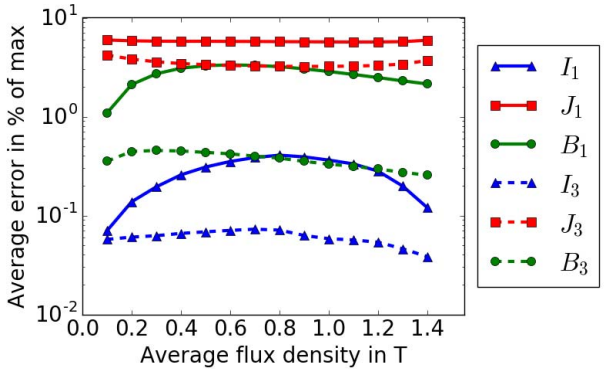


Fig. 17. Average errors of the MSFEM solution compared to the reference solution over a range of average flux densities using the nonlinear $B$–$H$ curve at 50 Hz, for both the first-order and third-order MSFEMs.

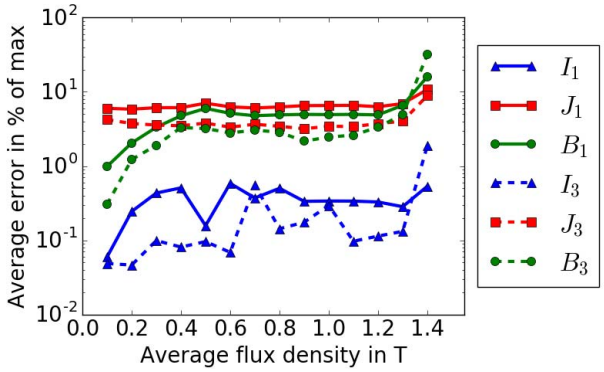


Fig. 18. Average errors of the MSFEM solution compared to the reference solution over a range of average flux densities using the Preisach model at 50 Hz, for both the first-order and third-order MSFEMs.

TABLE II
COMPUTATION TIMES

| | ref | $1^{st}$ order MSFEM | $3^{rd}$ order MSFEM |
|---|---|---|---|
| Nonlinear B-H curve | 441.3 s | 72.1 s | 79.8 s |
| Preisach model | 672.8 s | 61.9 s | 88.6 s |

flux densities, where saturation effects are not yet relevant and the material behaves roughly as if it was linear. For the simple nonlinear case, a decrease in the error can be observed for high average flux densities. This is due to the $B$–$H$ curve giving a very low $\mu$ in this range, resulting in a high penetration depth and a solution that can be approximated well by the MSFEM. When using a hysteresis model, the error becomes significantly larger for high flux densities with a strong saturation effect, compare [17].

In Figs. 19 and 20, the results of the same calculations for 10 Hz are presented. A comparison of Figs. 17 and 19 shows that for low frequencies, the first-order MSFEM is already sufficient to obtain nearly the same accuracy as the third-order method for 50 Hz. This is, again, because of the higher penetration depth in this setting which dampens the higher order components of the solution.

In Table II, the total computation times for both the reference solution and the MS are compared. Three full periods

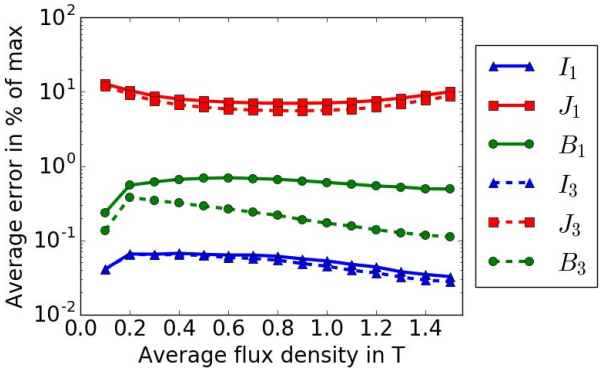


Fig. 19. Average errors of the MSFEM solution compared to the reference solution over a range of average flux densities using the nonlinear $B$–$H$ curve at 10 Hz, for both the first-order and third-order MSFEMs.

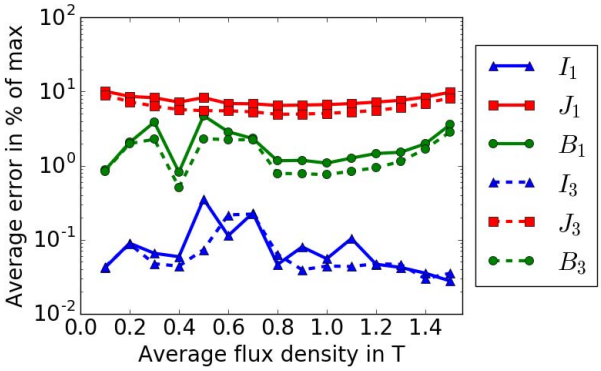


Fig. 20. Average errors of the MSFEM solution compared to the reference solution over a range of average flux densities using the Preisach model at 10 Hz, for both the first-order and third-order MSFEMs.

are simulated using 100 time steps per period. Third-order finite-element spaces are used for each function. The results demonstrate a significant decrease in computation time when using the multiscale method. Note that the studied problem is very small, which allows for the reference solution to be calculated in a feasible time. For a higher number of iron sheets, the reference solution would require much more degrees of freedom, while the MSFEM would not be affected significantly.

## VII. Conclusion

The eddy current problem with circuit coupling has been solved for a toroidal transformer, using the symmetry of the domain to reduce the problem to two dimensions. The numerical experiments demonstrate that the MSFEM is able to deliver reasonable results on a much coarser mesh compared to the standard FEM. The MSFEM has also been shown to be compatible with the Preisach model, allowing for a computationally cheap inclusion of hysteresis. In all numerical examples, the presented model shows an excellent accuracy in approximating the reference solution. Most importantly, the error of the MSFEM compared to the standard FEM is of the same order of magnitude for each studied material model, which is a strong indicator that the MSFEM is compatible with a wide range of models.

## Acknowledgment

This work was supported by the Austrian Science Fund (FWF) under Project P 27028 and Project P 31926.

## References

[1] K. Hollaus and J. Schöberl, "Some 2-D multiscale finite-element formulations for the eddy current problem in iron laminates," *IEEE Trans. Magn.*, vol. 54, no. 4, Apr. 2018, Art. no. 7401716.

[2] K. Hollaus and J. Schöberl, "A higher order multi-scale FEM with $A$ for 2-D eddy current problems in laminated iron," *IEEE Trans. Magn.*, vol. 51, no. 3, Mar. 2015, Art. no. 7402804.

[3] K. Hollaus, A. Hannukainen, and J. Schöberl, "Two-scale homogenization of the nonlinear eddy current problem with FEM," *IEEE Trans. Magn.*, vol. 50, no. 2, Feb. 2014, Art. no. 7010104.

[4] P. J. Leonard and D. Rodger, "Voltage forced coils for 3D finite-element electromagnetic models," *IEEE Trans. Magn.*, vol. 24, no. 6, pp. 2579–2581, Nov. 1988.

[5] G. Meunier, Y. Le Floch, and C. Guérin, "A nonlinear circuit coupled $t-t_0-\phi$ formulation for solid conductors," *IEEE Trans. Magn.*, vol. 39, no. 3, pp. 1729–1732, May 2003.

[6] O. Bíró, K. Preis, G. Buchgraber, and I. Ticar, "Voltage-driven coils in finite-element formulations using a current vector and a magnetic scalar potential," *IEEE Trans. Magn.*, vol. 40, no. 2, pp. 1286–1289, Mar. 2004.

[7] J. Schöberl and S. Zaglmayr, "High order Nédélec elements with local complete sequence properties," *Int. J. Comput. Math. Elect. Electron. Eng.*, vol. 24, no. 2, pp. 374–384, 2005.

[8] O. Bíró and K. Preis, "Finite element calculation of time-periodic 3D eddy currents in nonlinear media," in *Advanced Computing and Electromagnetics*, T. Homna, Ed. Budapest, Hungary: Elsevier, 1995, pp. 62–74. [Online]. Available: https://graz.pure.elsevier.com/en/publications/finite-element-calculation-of-time-periodic-3d-eddy-currents-in-n

[9] S. Steentjes, K. Hameyer, D. Dolinar, and M. Petrun, "Iron-loss and magnetic hysteresis under arbitrary waveforms in NO electrical steel: A comparative study of hysteresis models," *IEEE Trans. Ind. Electron.*, vol. 64, no. 3, pp. 2511–2521, Mar. 2017.

[10] E. D. Torre, *Magnetic Hysteresis*. Hoboken, NJ, USA: Wiley, 2000.

[11] Z. Szabó, I. Tugyi, G. Kádár, and J. Füzi, "Identification procedures for scalar Preisach model," *Phys. B, Condens. Matter*, vol. 343, nos. 1–4, pp. 142–147, 2004. [Online]. Available: http://www.sciencedirect.com/science/article/pii/S0921452603005672

[12] L. R. Dupre, G. Bertotti, and J. A. A. Melkebeek, "Dynamic Preisach model and energy dissipation in soft magnetic materials," *IEEE Trans. Magn.*, vol. 34, no. 4, pp. 1168–1170, Jul. 1998.

[13] D. Davino, A. Giustiniani, and C. Visone, "Fast inverse Preisach models in algorithms for static and quasistatic magnetic-field computations," *IEEE Trans. Magn.*, vol. 44, no. 6, pp. 862–865, Jun. 2008.

[14] L. R. Dupre, J. J. Gyselinck, and J. A. Melkebeek, "Complementary finite element methods in 2D magnetics taking into account a vector Preisach model," *IEEE Trans. Magn.*, vol. 34, no. 5, pp. 3048–3051, Sep. 1998.

[15] I. D. Mayergoyz, *Mathematical Models of Hysteresis and Their Applications*. Amsterdam, The Netherlands: Elsevier, 1991. [Online]. Available: https://www.sciencedirect.com/book/9780124808737/mathematical-models-of-hysteresis-and-their-applications#book-info

[16] G. Paoli, O. Biro, and G. Buchgraber, "Complex representation in nonlinear time harmonic eddy current problems," *IEEE Trans. Magn.*, vol. 34, no. 5, pp. 2625–2628, Sep. 1998.

[17] M. Petrun, S. Steentjes, K. Hameyer, J. Ritonja, and D. Dolinar, "Effects of saturation and hysteresis on magnetisation dynamics: Analysis of different material models," *Int. J. Comput. Math. Electr. Electron. Eng.*, vol. 34, no. 3, pp. 710–723, 2015. doi: 10.1108/COMPEL-10-2014-0286.